

# Impact of spatially varying transport coefficients in EMC3-Eirene simulations of W7-X and assessment of drifts

David Bold<sup>a</sup>, Felix Reimold<sup>a</sup>, Holger Niemann<sup>a</sup>, Yu Gao<sup>a</sup>, Marcin Jakubowski<sup>a</sup>, Carsten Killer<sup>a</sup>, Victoria R. Winters<sup>a</sup>, Nassim Maaziz<sup>a</sup> and the W7-X team<sup>b</sup>

<sup>a</sup>Max Planck Institute for Plasma Physics, Wendelsteinstr. 1, 17491 Greifswald, Germany

<sup>b</sup>See Pedersen et al 2022 [1] for the W7-X Team

E-mail: dave@ipp.mpg.de

18 July 2024

**Abstract.** Modelling the scrape-off layer of a stellarator is challenging due to the complex magnetic 3D geometry. The here presented study analyses simulations of the scrape-off layer (SOL) of the stellarator Wendelstein 7-X (W7-X) using spatially varying diffusion coefficients for the magnetic standard configuration, extending our previous study [2]. Comparing the EMC3-Eirene simulations with experimental observations, an inconsistency between the strike-line width (SLW) and the upstream parameters was observed. While to match the experimental SLW a particle diffusion coefficient  $D \approx 0.2 \text{ m}^2/\text{s}$  is needed,  $D \approx 1 \text{ m}^2/\text{s}$  is needed to get experimental separatrix temperatures of 50 eV at the given experimental heating power. We assess the impact of physically motivated spatially varying transport coefficients. Agreement with experimental data can be improved, but various differences remain. We show that drifts are expected to help overcome the discrepancies and, thus, the development of SOL transport models including drifts is a necessary next step to study the SOL transport of the W7-X stellarator.

## 1. Introduction

In order to operate fusion power plants based on the magnetic confinement concept the power flux on the plasma-facing surfaces needs to be controlled to prevent the overloading of structures. Predictive modelling of power loads, with high fidelity codes, such as EMC3-Eirene, will be necessary for the design of a next-step fusion device. Successful validation via comparison to existing experimental devices is required to ensure all important underlying physics is included in the code. One of these devices where we can do such a validation is Wendelstein 7-X (W7-X), an optimised stellarator with reduced neoclassical transport [1, 3, 4, 5, 6].

In contrast to tokamaks, the scrape-off layer (SOL) of W7-X is inherently three dimensional. W7-X features a 5-fold toroidal symmetry. Each of the 5 modules is in itself stellarator symmetric and can be split into two half modules. The SOL

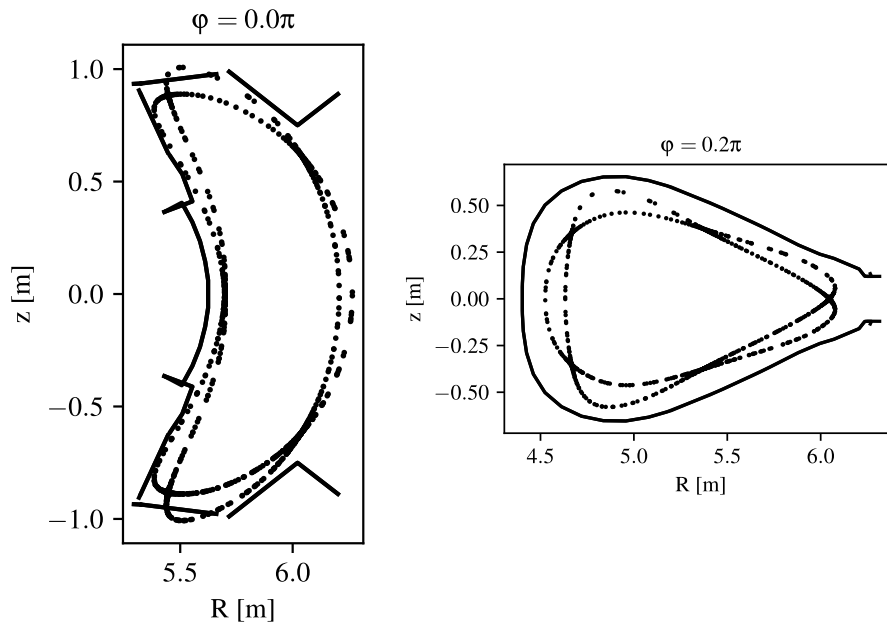


**Figure 1.** Shown are the islands at toroidal position  $\varphi = 0$  and  $\varphi = \pi/5 = 36^\circ$  as dots as well as the target structures used in the simulations, reproduced with kind permissions from [2].

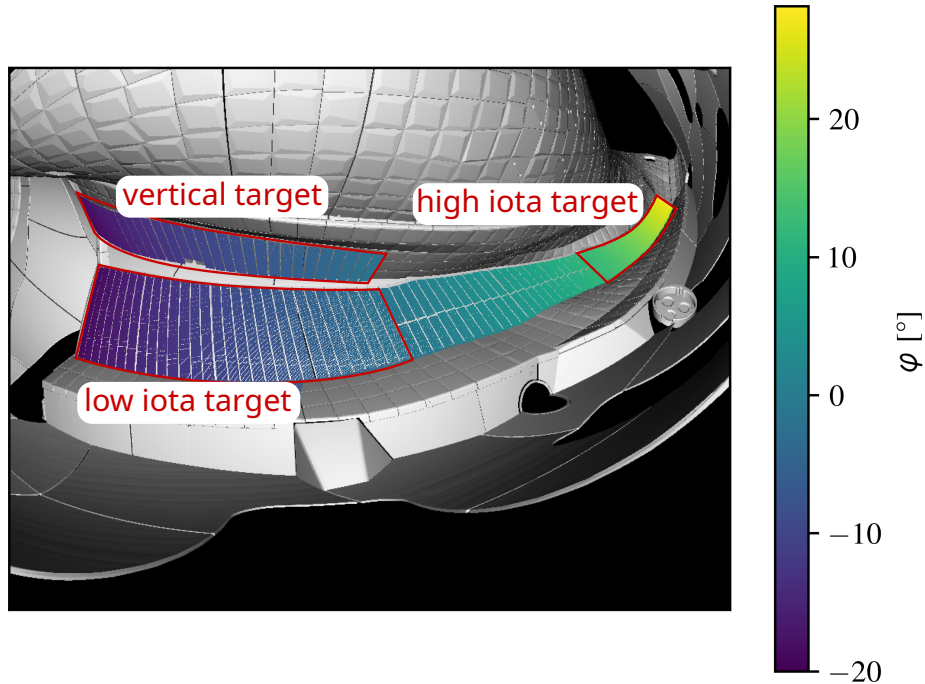


**Figure 2.** View into the divertor as seen from the IR camera. The divertor targets are shown colour coded. The colour represent the toroidal angle. The main, horizontal target is the larger of the two structures at the bottom. The vertical target is on the top, and only ranges to  $-20^\circ < \varphi < 0$ . In total 137 target structures, so called fingers, are visible, that have a toroidal extend of around  $0.5^\circ$ .

of W7-X features an island divertor, where in the standard configuration the 5 resonant islands are intersected by 10 divertor modules [7, 8, 9]. A plot of the islands and the intersection with the divertor is shown in fig. 1. The view of the thermography used later in this paper on to the divertor is shown in fig. 2.

The lack of toroidal symmetry makes the comparison of experimental measurements at different toroidal locations challenging. As a consequence, there is great need for 3D modelling, where synthetic diagnostics can be implemented to help understand whether differing diagnostic measurements are truly in disagreement or if differences are due purely to spatial variations in the plasma that are consistent with the implemented physics model. However, before such an analysis can be performed, it is critical to first validate the simulations, which itself requires diagnostic input covering as much of the SOL plasma domain as possible.

The anomalous cross-field transport in the SOL of fusion plasmas is often considered to be dominated by turbulence. In W7-X experiments, SOL turbulence and turbulent transport have been observed [10, 11, 12, 13]. Fully turbulent simulations of the full SOL are computationally extremely challenging and not available for 3D stellarator geometries yet. Simpler models are generally used, such as fluid transport codes [14]. There the turbulence is effectively represented by anomalous diffusion coefficients. The simplest diffusion model features a spatially constant diffusion coefficient. Spatially varying diffusion coefficients give significantly more freedom in matching data and have been used in tokamak simulations in the past [15, 16, 17]. However, finding appropriate distributions of the diffusion coefficient is challenging due to the large parameter space. To limit the parameter space, the coefficients can, for example, be motivated by experimental observations, theoretical predictions, or turbulence simulations [17].

This work validates the diffusion-based anomalous transport in the absence of drifts in the model in EMC3-Eirene [18, 19] by extending the isotropic diffusion scan [2] to spatially varying transport coefficients. The simulations are compared to experimental data from W7-X's infra-red heat-flux diagnostic and the reciprocating electric probes. In particular, the radial profiles of electron temperature and density, the strike-line width and toroidal distribution of heat-flux onto the divertor will be compared. The analysis presented here is restricted to the magnetic standard configuration.

The scope of the paper is to assess the impact of spatially varying and physically motivated transport coefficients rather than exhaustive variations to fit experimental data. The general impact of the applied variations is discussed to elucidate the role of the variation.

This paper is organized as follows: Section 2 the diffusion coefficient profiles are introduced and motivated. In section 3 the experimental conditions are summarized, a detailed description is given in ref. [2]. In section 4, the simulations are presented. Section 5 summarises and discusses the results, here it is seen that a spatially varying diffusion coefficient can improve matching downstream and upstream conditions in the magnetic standard configuration. The main conclusions are presented in the final section.

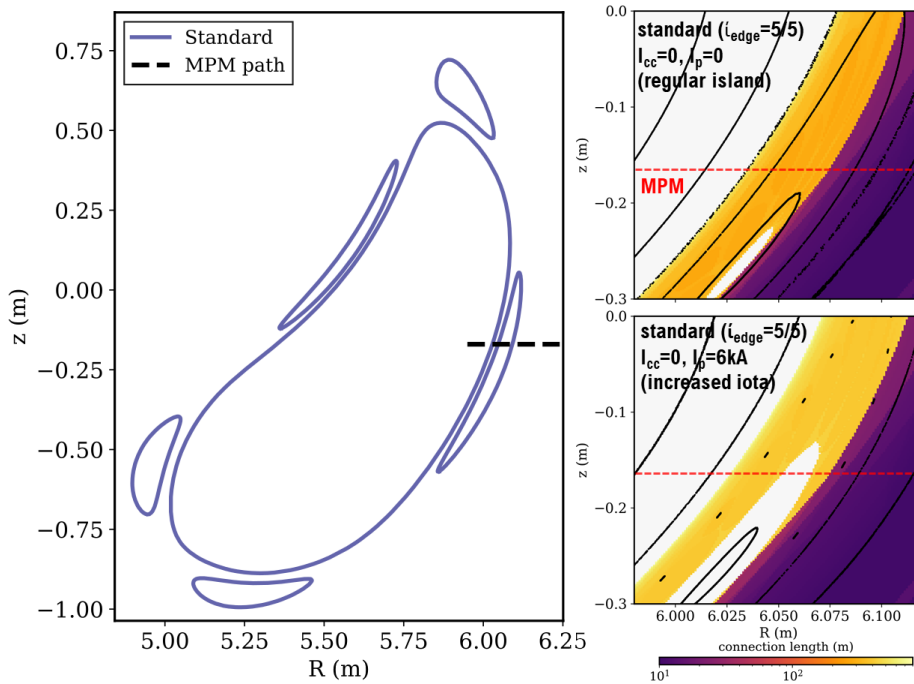


**Figure 3.** Position of the MPM diagnostic, showing the islands and last-closed flux surface (LCFS) on the left, and a plot of the connection length on the right, for the ideal case of no toroidal plasma current, as assumed in the simulations, on the top and for a finite plasma current of 6 kA on the bottom. Reproduced with kind permission from [23].

## 2. Method

### 2.1. W7-X diagnostics

As in previous work [2], two diagnostics are used for comparison to simulation data: one is located downstream at the divertor targets and the other upstream. Both downstream and upstream parameter comparisons are important to determine if the EMC3-Eirene simulations successfully reproduce features across the entire SOL. The downstream measurement used is the infra-red (IR) camera system [20], which fully covered the area of 9 out of 10 divertors in the previous experimental campaign OP 1.2b. The view onto the target is shown in fig. 2.

The temperature is derived from the spatial distribution of the IR radiation. The heat-flux is calculated by the evolution of the temperature profiles using the two-dimensional thermal model THEODOR [21]. This heat-flux is used to assess the validity of the employed SOL transport model in EMC3-Eirene as the heat-flux has a high spatial resolution. The spatial resolution is around 3 mm and the noise level is around  $0.25 \text{ MW/m}^2$ .

The second diagnostic used for comparison are reciprocating Langmuir probes mounted on the Multi-Purpose Manipulator (MPM) which provide profiles of electron temperature and density [22, 23]. This provides plasma parameters upstream and, thus, complements the downstream comparison provided by the heat-flux measurements at the divertor. Unlike the infra-red diagnostic the MPM is only present in one half module and, therefore, does not give a direct measurement of up-down asymmetries [9] or field errors [24]. The path of the MPM is shown in fig. 3.

It is crucial to include measurements from different locations, to constrain the model. Otherwise (de)validation of a model is not possible. Especially with a raising number of degrees of freedom in the model, sufficient amount of experimental data needs to be used for comparison.

### 2.2. Heat-Flux distribution analysis

The strike-line width and amplitude are used to compare the heat-flux profiles between experiment and modelling. For all toroidal locations of each target, the poloidal position, amplitude and strike-line width is determined, by a fit of the main heat-flux peak along the strike-line. For a detailed description of the mapping and analysis of the heat-flux, see our previous work [2].

Fig. 4 shows the connection length ( $L_c$ ) mapped to the target regions along with a typical heat load pattern. Fig. 5 shows the maximum  $L_c$  as a function of toroidal angle for the horizontal and vertical target, see fig. 2. Regions of very long connection length  $> 500 \text{ m}$  indicate the location of the main strike-line formed by the intersection of the edge of the island on the divertor target plates. For the standard configuration, the main strike-line is on the horizontal target, but, also on the vertical target long connection lengths are observed.

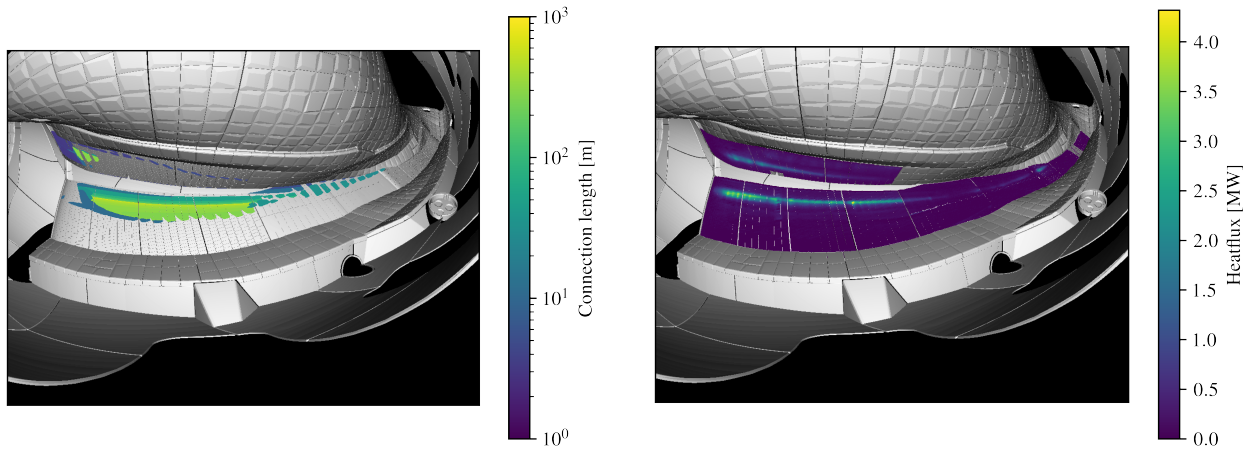


**Figure 4.** Shown on the left is a plot of the connection length mapped on to the target. In grey the target regions where no traced field line ended are shown. On the right is a plot of the heat-flux on the divertor at  $t = t_1 + 3.3$  s for shot #20180920.009. The main strike-line is on the horizontal target  $\varphi \approx 0^\circ$ , roughly in agreement with the long connection lengths. Additional heat loads on the horizontal target around  $\varphi \approx 13^\circ$  as well as the vertical target are visible.

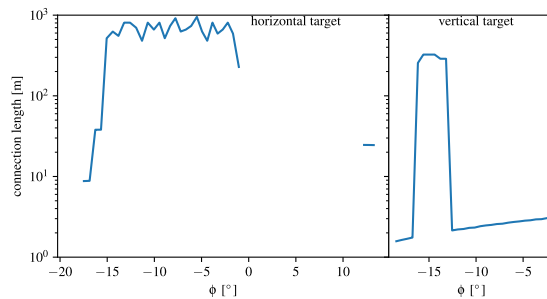


**Figure 5.** The maximum of connection length as shown in fig 4 as a function of toroidal angle.

### 2.3. EMC3-Eirene

EMC3-Eirene has been used to simulate the scrape-off layer in the current work. EMC3-Eirene is a Monte Carlo fluid transport and kinetic neutral code, that is capable of handling complex geometries, such as those commonly encountered in the SOL of stellarators. It has already been used in the past to model the edge of W7-X [19, 14, 2]. While EMC3-Eirene does capture some of the observations in experiments, especially global trends [14, 19], there is still disagreement in local parameters [25, 2].

EMC3-Eirene does include parallel transport in the form of advection as well as viscosity and parallel heat diffusivity. Perpendicular transport included in EMC3-Eirene features anomalous diffusion based on some given particle and heat diffusion coefficients, that can be spatially varying [18, 16]. EMC3-Eirene does not require nested flux-surfaces and is only “aware” of the local magnetic geometry, i.e. it is ignorant of island flux surfaces. For this reason the perpendicular diffusion is uniform in flux-surface perpendicular and bi-normal direction. Drifts are not included in EMC3-Eirene.

The simulations are analysed using the same procedure as described in [2]. Both experimental as well as simulation data have been fitted using the same routines to produce a more consistent data set for comparison.

## 3. Experimental data

Despite the qualitative modelling approach, the analysis should be done in realistic conditions and with reference to experimental data. The W7-X experiments #20180920.009 and #20180920.013 have been analysed and are compared to the simulations. They are part of a density scan with an input power of 4.7 MW ECRH. For a more detailed description of the experiments, see our previous work [2].

The line integrated density was  $4 \cdot 10^{19} \text{ m}^{-2}$  and  $6 \cdot 10^{19} \text{ m}^{-2}$ . These low and medium density cases were selected as they feature a low radiative fraction  $f_{rad} = P_{rad}/P_{heat}$  of 0.15 to 0.35. This allows us to focus on the effect of heat transport on the target heat load distribution, reducing the additional impact of radiation as volumetric loss.

The data for the MPM comes from the experiments #20181010.008, #20181010.021, #20181010.022 and #20181010.016. They are similar to the other two experiments and then density is in the range of  $4.5 \dots 6 \cdot 10^{19} \text{ m}^{-2}$ .

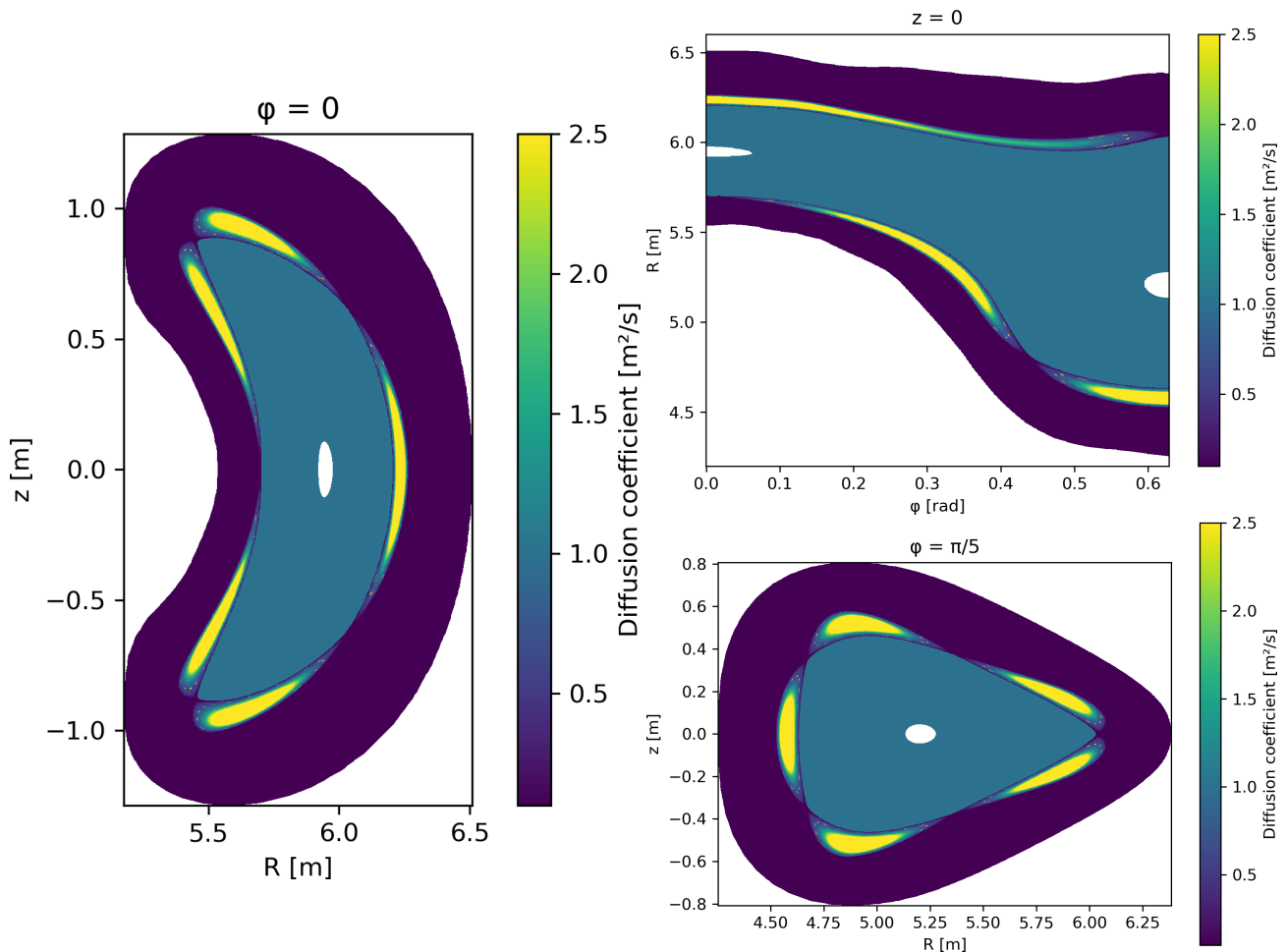


**Figure 6.** Plot of scenario B: diffusion based on experimental data featuring radial-poloidal variation. On the left is a cut at  $\varphi = 0$ , on the right top at  $z = 0$  and on the right bottom  $\varphi = \pi/5 = 36^\circ$ . The diffusion is set to  $D = 1 \text{ m}^2/\text{s}$  in the core region for numerical stabilities of the boundary conditions. Further outside a background of  $D = 0.1 \text{ m}^2/\text{s}$  is used, and enhanced towards the centre of the islands.

## 4. Simulations

In order to decrease the discrepancies observed in the previous study [2], where low values of the diffusion coefficients were needed to match the strike-line with, and high values were needed to reduce the upstream temperature, spatially varying diffusion coefficients are assessed here for their potential to reconcile the upstream and downstream measurements. These scenarios are not intended to model the SOL of W7-X in a realistic way, but rather to measure the impact of the changes onto the synthetic diagnostics, test their ability to improve agreement, and elucidate what transport aspects are changed or not. Another question addressed here is whether the different transport models could be distinguished by diagnostics in experiments via specific features or scalings.

### 4.1. Spatially varying diffusion

The simulations presented here use spatially varying heat and particle diffusion coefficients, which are implemented in EMC3-Eirene. In addition to scenario A: constant diffusion presented in ref. [2], two spatial variation patterns were implemented in this work: scenario B, motivated by experimental observations and scenario C, motivated by turbulence characteristics. Scenario B is shown in fig. 6. The transport is suppressed at the separatrix and enhanced towards the island centres. The distribution is motivated by experimentally observed heat-fluxes, as the narrow strike-line requires a low transport coefficient at the separatrix, but for agreement with other diagnostics measuring away from the strike-line, such as the MPM, higher transport coefficients are required [19]. Thus, combining a low perpendicular transport value at the separatrix and a higher value towards the centre of the island can better satisfy both conditions. It will lead to a tightly confined power carrying layer, focusing the parallel heat-flux towards the divertor while broadening the profiles upstream towards the O-point. Fig. 6 on the right shows the coefficients at  $z = 0$ . The variation along the toroidal direction  $\varphi$  in fig. 6  $z = 0$  is due to the poloidal contribution of the magnetic field, as the variation of  $D$  is aligned with the magnetic field and the island rotates around the LCFS.

Scenario C, motivated by turbulent transport drivers is shown in fig. 7. In this scenario the transport is enhanced in the outer bean shape, where a Gaussian perturbation has been added to a constant background. The outer bean shape features

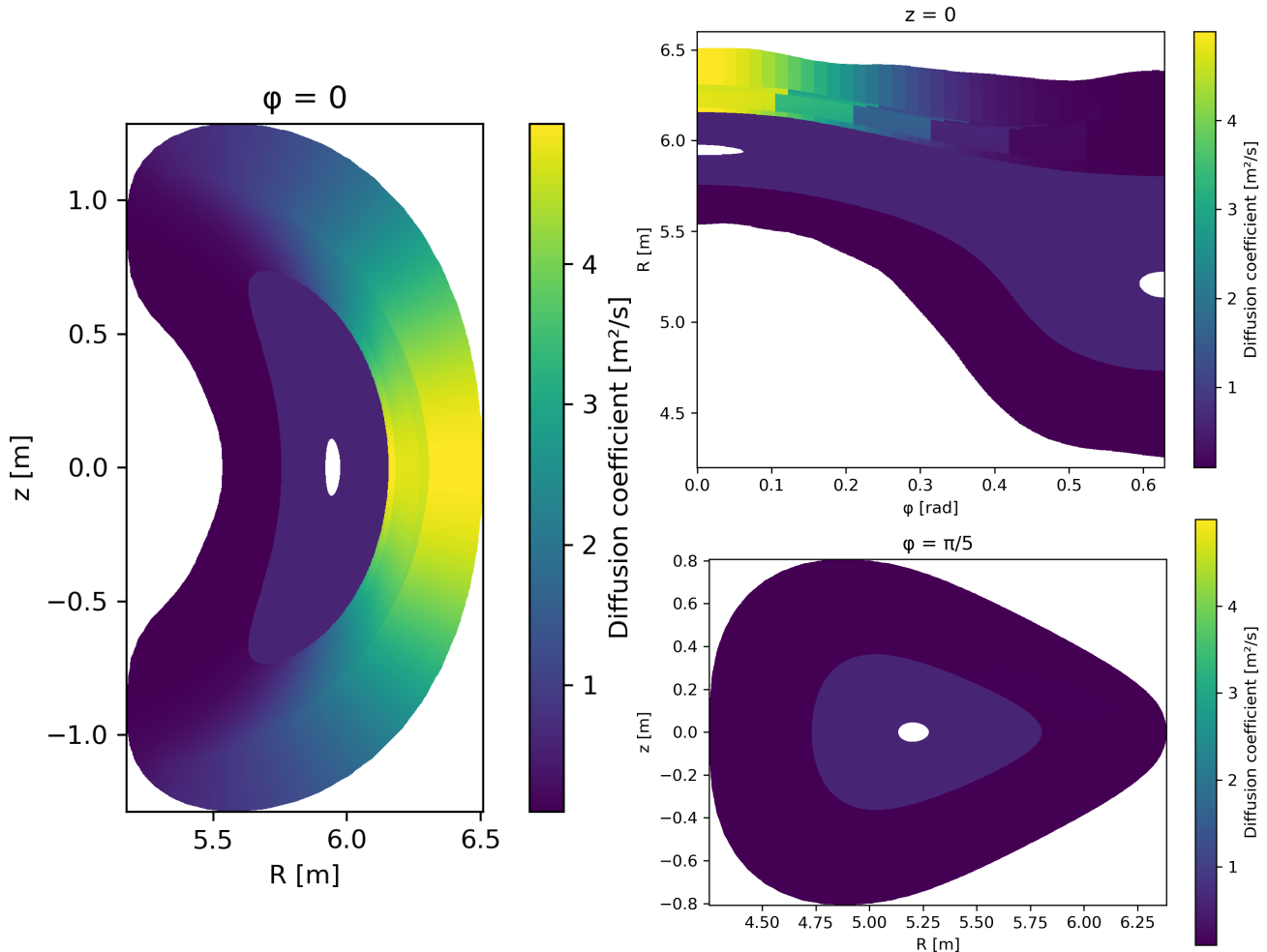


**Figure 7.** Plot of scenario C: diffusion based on turbulence metrics featuring a poloidal-toroidal variation. On the left is a cut at  $\varphi = 0$ , on the right top at  $z = 0$  and on the right bottom  $\varphi = \pi/5 = 36^\circ$ . The diffusion is enhanced in the core region for numerical stabilities of the boundary conditions. Further outside a background of  $D = 0.1 \text{ m}^2/\text{s}$  is used and enhanced in the outer bean shape.

the largest values of bad curvature, which is a significant driver for turbulent transport in the SOL [10, 26]. Thus, this set of simulations mimics in a naïve way the effect of turbulent transport and probes the impact of toroidally localised power flux into the SOL, similar to ballooning type assumptions in tokamak modelling.

In all cases the heat diffusion coefficient  $\chi$  is set to  $\chi = 3 \cdot D$ , i.e. scaled with the particle diffusion coefficient. Note that the resulting transport  $q_\perp \propto n\chi$ , i.e. has a density dependence even for constant  $\chi$ .

#### 4.2. Simulation parameter

The scrape-off layer of W7-X has been modelled using EMC3-Eirene. For this the upstream density was scanned. The simulation relies on the stellarator symmetry of W7-X's standard geometry and, therefore, only one half module is modelled. Ideal coils are used and, thus, no error field effects are included. Drifts are not included.

Input parameters are set consistently with [2]. The input heating power within the simulation domain (one half module) was set to be 470 kW, leading to a total of 4.7 MW for the whole device. The power was distributed evenly between ions and electrons, and enters the domain at the core boundary. The observed power on the divertor is up to 352 kW - giving a total power of  $\approx 3.5 \text{ MW}$  on all divertors. The radiation was fixed to 1 MW, achieved via carbon impurity radiation, giving a radiation fraction  $f_{rad} \approx 21\%$ . In the experiment the radiation fraction varies from 15% to 35%. The low  $f_{rad}$  was selected to avoid a dominant effect of the radiation losses.

The upstream density was set to a fixed value of  $n_{e,sep} = 1 \cdot 10^{19} \text{ m}^{-3}$  and  $n_{e,sep} = 3 \cdot 10^{19} \text{ m}^{-3}$ . The cases are roughly in the range of the experiments. No pumping and fuelling is included in the simulations and, therefore, particle balance is achieved via scaling of the recycling flux to the amount needed for the fixed upstream density value.

The same magnetic field configuration was used in simulation as in experiment: the standard magnetic field configuration, featuring a 5/5 island chain in the SOL.

For each diffusion coefficient setup described in sec. 4.1, a scan in density and in magnitude of diffusion coefficient was performed. The case with uniform diffusion coefficients (scenario A) is also included for reference.

Fig. 8 shows plots of the electron density and temperature distribution of a simulation, where the diffusion coefficient was set to  $D = 0.1 \dots 0.4 \text{ m}^2/\text{s}$  from scenario B and the upstream density was set to  $n_{e,sep} = 1 \cdot 10^{19} \text{ m}^{-3}$ . The density shows

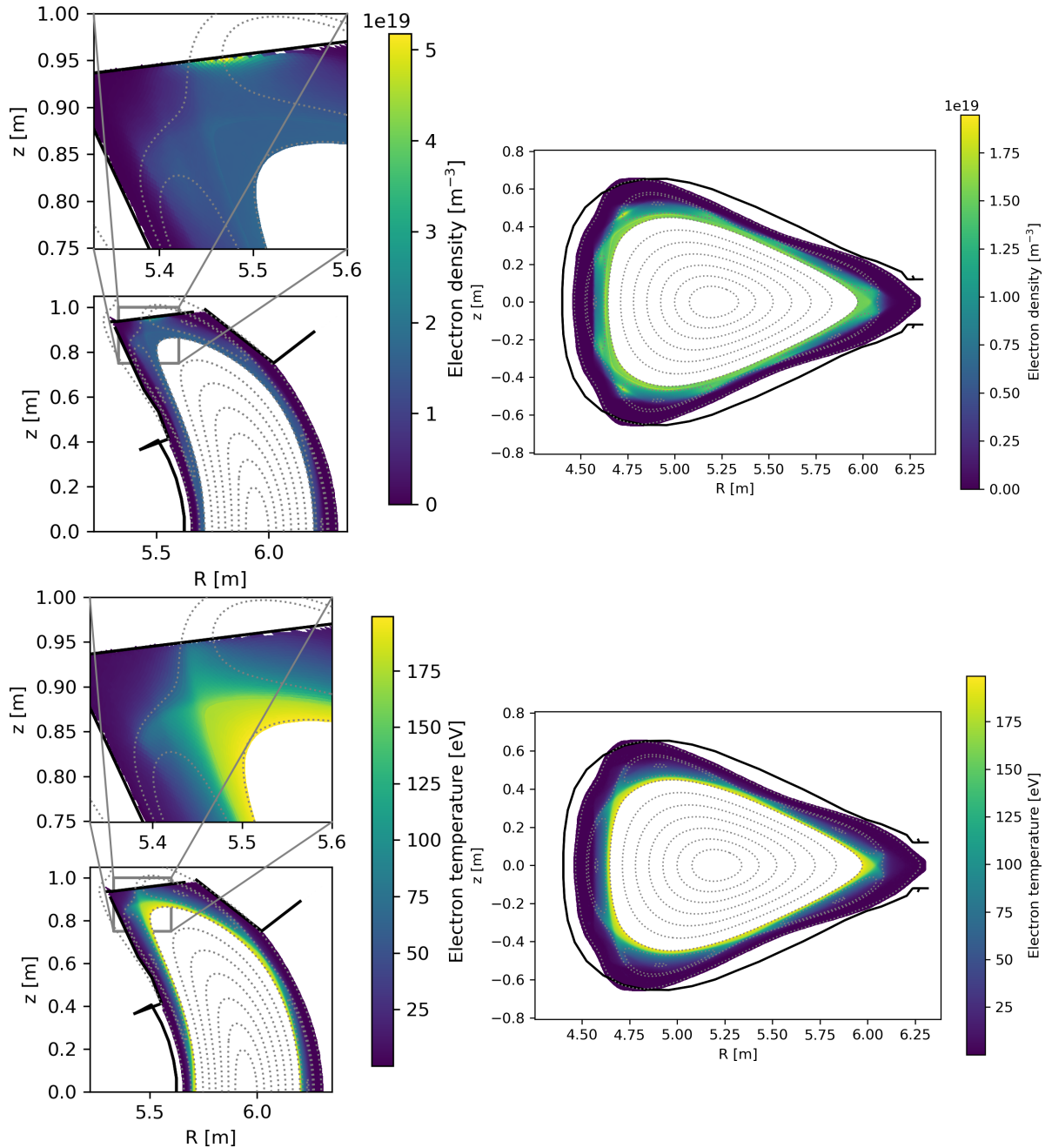


**Figure 8.** Density (top) and electron temperature (bottom) profiles for scenario B at  $n_{e,sep} = 1 \cdot 10^{19} \text{ m}^{-3}$  with  $D = 0.1 \dots 0.4 \text{ m}^2/\text{s}$  at the bean shape, at  $\varphi = 0$  (left) and the triangular shape, at  $\varphi = \pi/5 = 36^\circ$  (right). Shown in black are the plasma facing components and as grey dotted lines some flux surfaces.

a peak just in front of the target, which is observed in all simulations. This can be seen at toroidal angle  $\varphi = 0$ , where the upper and lower target plates are visible. At the triangular shape ( $\varphi = \pi/5 = 36^\circ$ ) no target plates are present and, thus, also the density is not as strongly peaked as in the presence of targets, where recycling is happening. Note the difference in the colorbar for the density. In this case the average electron temperature at the separatrix is around 150 eV. The average separatrix electron temperature is for all cases analysed here below 200 eV. Experimentally, separatrix electron temperatures were between 30 and 100 eV. This deviation will be discussed later in sec. 4.5.

### 4.3. Toroidal distribution

The heat-flux on each target finger, as introduced in fig. 2, is spatially integrated, giving the toroidal distribution of the heat-flux. The toroidal distribution for scenario A is shown in fig. 9 on top. For the non-constant diffusion coefficients the toroidal power distribution for each density level is shown in fig. 9 on the middle and bottom. The general trends are similar. For low diffusion coefficients, with increasing density less power is deposited on the low iota target (horizontal target at  $\varphi \approx 0^\circ$ ), and more on the high iota target ( $\varphi \approx 12^\circ$ ) as well as the vertical target. The power on the low iota target is for low density and low diffusion coefficients peaks at  $\varphi \approx -2^\circ$  and only with higher density and diffusion a more flat distribution on the low iota target is observed. Peaking at  $\varphi \approx -17^\circ$  as in experiments is, in general, not observed in the simulations. While in

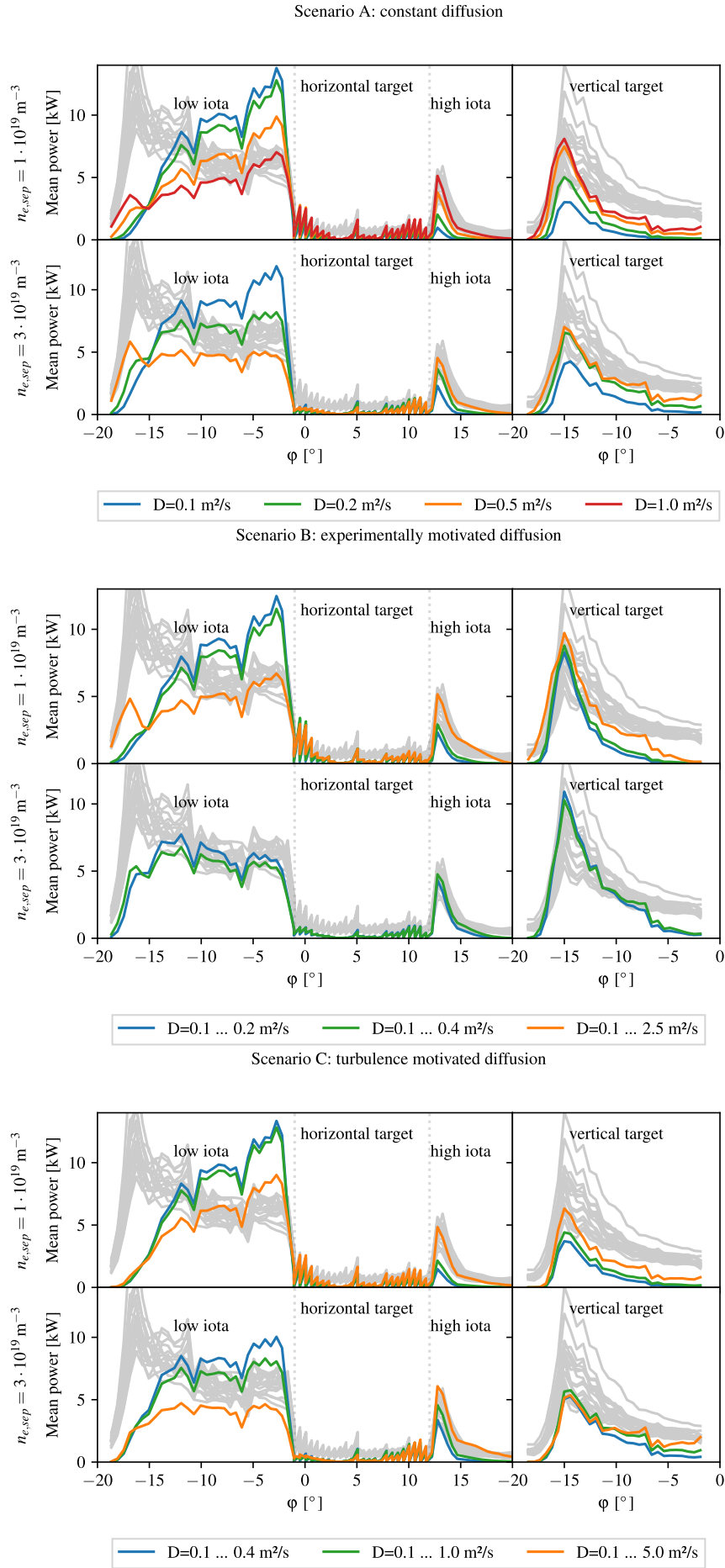


**Figure 9.** Plot of the power per finger for simulations. On the top are the results for scenario A: constant diffusion coefficients. In the middle are the results for scenario B: motivated by experimental observation. On the bottom are the results for scenario C: motivated by bad curvature. The experimental data is shown in light grey.



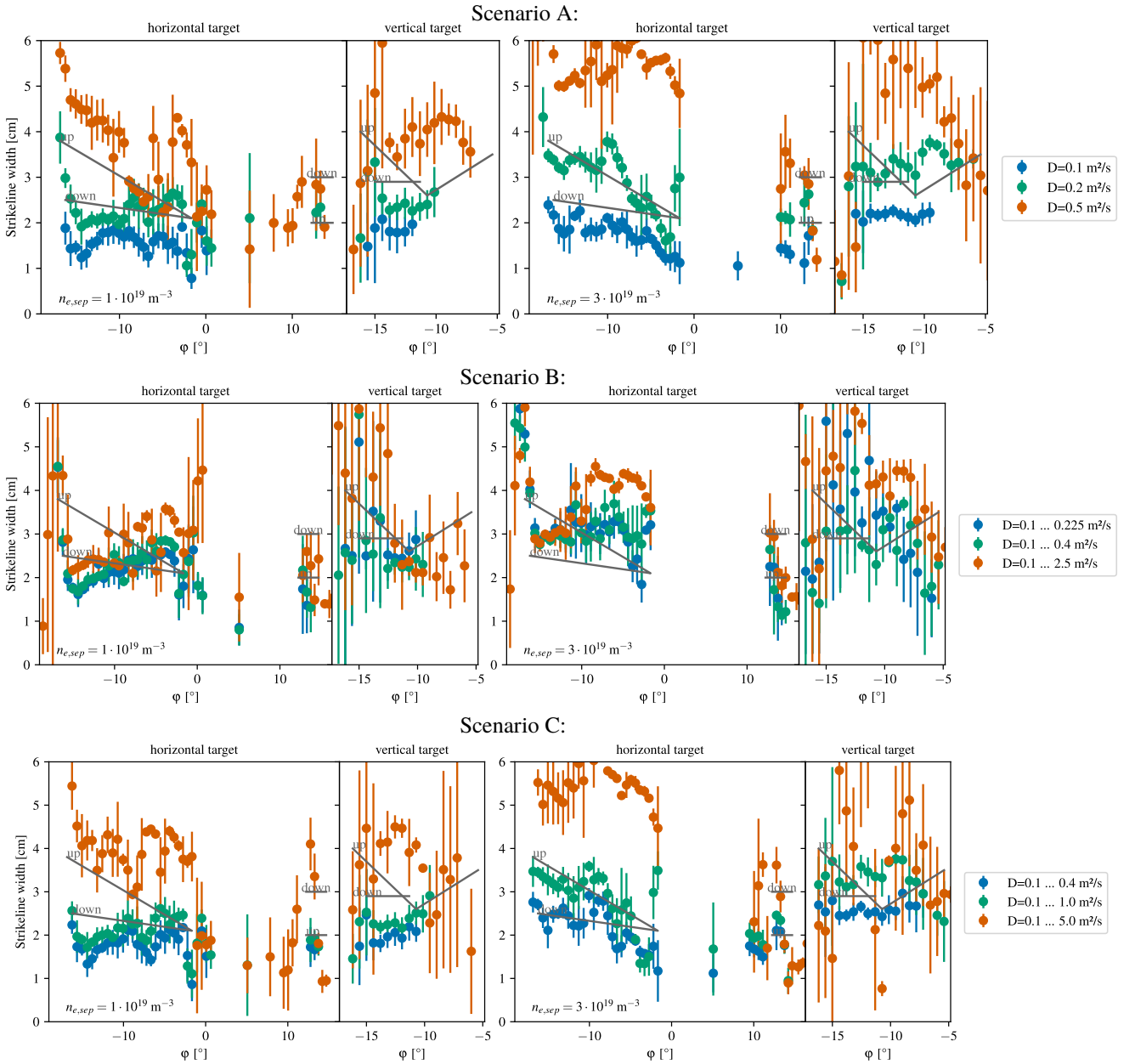


**Figure 10.** Mean of the strike-line width as a function of the fingers, as introduced in fig. 2. The power on the finger is colour coded. Simulation results for a constant diffusion  $D = 0.1 \dots 0.5 \text{ m}^2/\text{s}$  on top, results for scenario B introduced in fig. 6 in the middle and results for scenario C introduced in fig. 7 on the bottom. On the left are the results for  $n_{e,\text{sep}} = 1 \cdot 10^{19} \text{ m}^{-3}$  and on the right for  $n_{e,\text{sep}} = 3 \cdot 10^{19} \text{ m}^{-3}$ . The grey lines show the estimates for the low density case from ref. [2].

the  $n_{e,\text{sep}} = 1 \cdot 10^{19} \text{ m}^{-3}$  cases the peak is around  $\varphi \approx -2^\circ$ , the toroidal profiles are more flat for the  $n_{e,\text{sep}} = 3 \cdot 10^{19} \text{ m}^{-3}$  cases. In general scenario B for  $n_{e,\text{sep}} = 3 \cdot 10^{19} \text{ m}^{-3}$  matches best the experimental results. The main disagreement is the missing peak at  $\varphi \approx -17^\circ$ .

In all cases an increase in density or diffusion coefficient causes:

- flattening of the toroidal distribution
- more power on the vertical target
- more power on the high iota target
- less power on the low iota target

This is in agreement with experiments, where the trends are also observed for increasing density.

#### 4.4. Strike-line

The width of the strike line is of particular interest, as this influences the area over which the heat is distributed and, thus, also the peak heat-flux that the divertor has to withstand. Besides this more practical question, the strike-line width gives also insight into the transport. Fig. 10 shows on top the fitted strike-line width for separatrix densities  $n_{e,\text{sep}} = 1 \cdot 10^{19} \text{ m}^{-3}$

and  $n_{e,sep} = 3 \cdot 10^{19} \text{ m}^{-3}$  with a diffusion coefficient scan in the range  $D = 0.1 \dots 0.5 \text{ m}^2/\text{s}$  for scenario A: constant diffusion. The experimentally observed density is likely between  $n_{e,sep} = 1 \cdot 10^{19} \text{ m}^{-3}$  and  $n_{e,sep} = 3 \cdot 10^{19} \text{ m}^{-3}$ , as will be later discussed based on MPM data in sec. 4.5.

For the lowest  $D = 0.1 \text{ m}^2/\text{s}$  the strike-line width is  $1 \dots 2 \text{ cm}$  on the low iota target, and, thus, smaller than the experimentally observed ones as indicated by the grey line. The two grey lines are measurements for the upper and lower divertor. Differences are expected due to drifts. For  $D = 0.2 \text{ m}^2/\text{s}$  the strike-line width is  $2 \dots 3 \text{ cm}$  matching most closely to the experiment, while for  $D = 0.5 \text{ m}^2/\text{s}$  the strike line width is in the range of  $2 \dots 5 \text{ cm}$  and, thus, a bit larger than observed.

The peak on the high iota target, on the horizontal target at  $\varphi \approx 12^\circ$ , agrees with experiment for  $D \geq 0.5 \text{ m}^2/\text{s}$  and  $n_{e,sep} = 1 \cdot 10^{19} \text{ m}^{-3}$  spatially constant diffusion coefficient values. For the  $n_{e,sep} = 3 \cdot 10^{19} \text{ m}^{-3}$  cases,  $D \geq 0.2 \text{ m}^2/\text{s}$  matches.

The strike-line widths for the spatially varying diffusion coefficients are shown in fig. 10 in the middle for scenario B: diffusion motivated by experiment and on the bottom for scenario C: diffusion motivated by turbulent transport. In order to change the strike-line width in the low iota target, a significant variation of  $D$  is needed. In contrast, the strike-line width on the vertical target is more sensitive to an enhanced transport in the island then on the horizontal target. The increased strike-line width coincides with an increased power load on the vertical target.

From the strike-line width on the low iota target, in scenario B: motivated by experimental observations, shown in fig. 10, the  $D = 0.1 \dots 2.5 \text{ m}^2/\text{s}$  case agrees with the experimental observations. For scenario C, the experimental strike-line width on the low iota target lies between the  $D = 0.1 \dots 1.0 \text{ m}^2/\text{s}$  and the  $D = 0.1 \dots 5.0 \text{ m}^2/\text{s}$  case. Thus, for all scenarios we can find cases that give similar strike-line widths than observed in experiments, all of which feature low level of  $D \approx 0.1 \text{ m}^2/\text{s}$  around the island separatrix.

#### 4.5. Upstream data

To further compare the output of the models to experimental data, upstream data is critical. As introduced in sec. 2.1, the MPM can measure the density and temperature in the SOL, outside of the separatrix. Due to the separation from the targets, this gives a more complete picture, allowing to (de)validate the transport model.

Figure 11 shows the density and temperature along the line of sight of the MPM diagnostic. Although no experimental MPM data is available for program #20180920.009 and #20180920.013, similar programs with MPM data exist and are used as an upstream comparison to simulation. The simulation results, for both spatially constant and spatially varying diffusion coefficients, are plotted as lines in fig. 11. The simulations that match the strike-line width best are plotted as lines, lower  $D$  distributions are dotted and higher ones are dashed, for all three scenarios.

All simulations show essentially monotonic behaviour in the temperature and the density profiles. Even though the transport coefficient feature significant changes, the profiles look relative similar. This is in contrast to the experimental data, where the density shows a monotonic, roughly exponential decay in the shadow region  $R > 6.08 \text{ m}$  but further inside the gradient vanishes. Towards the centre of the island the density peaks in some cases, but not in all. The temperature profiles show less variation. They show a monotonic trend in the shadowed region similar to the density. In the region of longer connection length, towards the O-point of the island, a hollow temperature profile is observed. The hollow temperature is not observed in any of the simulations.

The separatrix density is an input parameter for the simulations. As such simulations matching best the experimental case can be chosen. For all diffusion cases,  $n_{e,sep} = 1 \cdot 10^{19} \text{ m}^{-3}$  seems to underestimate the density, while  $n_{e,sep} = 3 \cdot 10^{19} \text{ m}^{-3}$  seems to overestimate the density. Quantifying which case matches best, or which density would match best, is not well defined as the profiles do not match qualitatively. The density for scenario A,  $n_{e,sep} = 3 \cdot 10^{19} \text{ m}^{-3}$  matches very well in the target shadow, while, depending on the experimental measurement, the  $n_{e,sep} = 1 \cdot 10^{19} \text{ m}^{-3}$  case matches reasonably well towards the O-point. Scenario B shows, like the experimental data, a drop in the density profile but further out around  $R \approx 6.10 \text{ m}$ . This kink is caused by a change in  $D$ , from the increased value in the centre of the island to  $D = 0.1 \text{ m}^2/\text{s}$  outside the island. For  $R < 6.10 \text{ m}$  the profile is roughly linear, while further outside an exponential profile is simulated. For the experiments, the drop is  $R \approx 6.08 \text{ m}$ , with an exponential behaviour outside.

For the temperature, all simulations feature a too high temperature towards the island centre. Not shown here is the separatrix, where the temperature in all simulations increases further towards the separatrix up to  $200 \text{ eV}$ , while experimentally values below  $100 \text{ eV}$  are measured. Scenario B shows the lowest separatrix temperature. Due to the large fall-off length, the temperature is higher further out than observed by the other simulations.  $D = 0.1 \text{ m}^2/\text{s}$  for scenario A might appear to show good agreement, as it features the lowest temperature at  $R \approx 6.06 \text{ m}$ , but the temperature at the separatrix is the highest of all shown simulations. Similar to the density profile, the temperature profile of scenario B shows a kink, featuring a stronger fall off outside. In general, with increasing  $D$  the separatrix temperature decreases, and the fall-off-length increases. The impact of the transport coefficient on the simulated profiles will be analysed and discussed in the following section.

#### 4.6. Summary

The allow for a stream lined discussion of the findings, a short summary is given here.

- Increasing  $D$  or  $n$  increases the strike-line width. Depending on the distribution the dependency is weak.

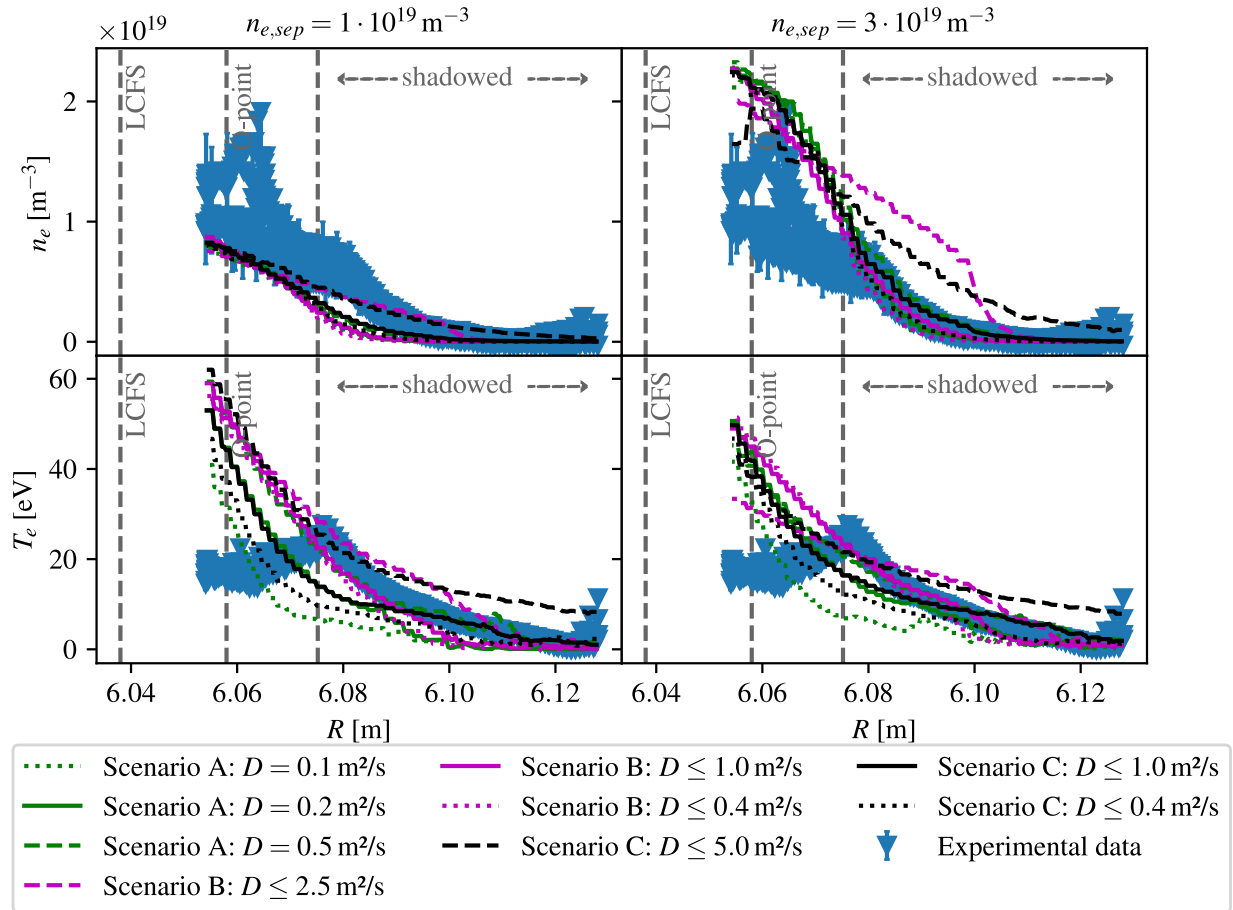


**Figure 11.** Plot of electron density (top row) and electron temperature (bottom row) as a function of the radial position. Shown is a 1D cut along the path of the MPM diagnostic [23, 22]. The experimental data from the MPM diagnostic is shown as symbols. The differences in the MPM measurements are expected as the data is from different experiments. Simulation data for  $n_{e,sep} = 1 \cdot 10^{19} \text{ m}^{-3}$  is shown on the left and for  $n_{e,sep} = 3 \cdot 10^{19} \text{ m}^{-3}$  on the right hand side. Continuous lines are the simulations for the best matching diffusion based on strike-line width for the given spatial distribution. Dotted lines denote lower diffusion, i.e. more narrow strike-line width and dashed lines denote higher diffusion values. For scenario A: constant diffusion  $D = 0.1 \text{ m}^2/\text{s}$  is plotted as green dotted,  $D = 0.2 \text{ m}^2/\text{s}$  as green line (best match based on strike-line width) and  $D = 0.5 \text{ m}^2/\text{s}$  as green dashed. Note that the temperature for  $D = 0.1 \text{ m}^2/\text{s}$  is lower in the plotted regime, the gradient is higher and the separatrix temperature is the highest for the low diffusion value. For scenario B: diffusion motivated by experiment,  $D = 0.1 \dots 0.4 \text{ m}^2/\text{s}$  is shown as magenta dotted,  $D = 0.1 \dots 2.5 \text{ m}^2/\text{s}$  as magenta line (best match based on strike-line width) and  $D = 0.1 \dots 10 \text{ m}^2/\text{s}$  as magenta dashed. For scenario C: diffusion motivated by turbulence,  $D = 0.1 \dots 1 \text{ m}^2/\text{s}$  as black dotted and  $D = 0.1 \dots 5 \text{ m}^2/\text{s}$  as black line (best match based on strike-line width). The point magnetically closest to the O-point is around  $R = 6.05$  m while the shadowed area is around  $R > 6.075$  m.

- Increasing  $D$  or  $n$  changes the toroidal heat-flux distribution. In general the distribution on the low iota target gets less peaked, and more power is reaching the high iota and vertical target.
- There is a mismatch in the target shadow region, e.g. on the horizontal target around  $\varphi \approx -17^\circ$  and  $0^\circ \lesssim \varphi \lesssim 10^\circ$  and on the vertical target around  $\varphi \approx -17^\circ$  as well as  $\varphi \approx -5^\circ$ .
- In the experiment the target heat flux peaks around  $\varphi \approx -17^\circ$  and decreases towards  $\varphi \approx -2^\circ$ , while in the simulations it peaks at  $\varphi \approx -2^\circ$  and decreases towards  $\varphi \approx -17^\circ$ . As the distribution becomes more flat with higher  $D$  or  $n$ , the difference reduces.
- The upstream measurements show a vanishing gradient at the point closest to the O-point, the simulations show in all cases a monotonic decrease with radius.
- The monotonic behaviour in the radial profiles is resilient to the tested variation in the transport coefficients.
- The upstream temperature observed in simulations is in all cases too high, even for higher density cases.

## 5. Discussion

In this section the results from sec. 4 will be discussed. Note that a short summary of the findings is given in sec. 4.6.

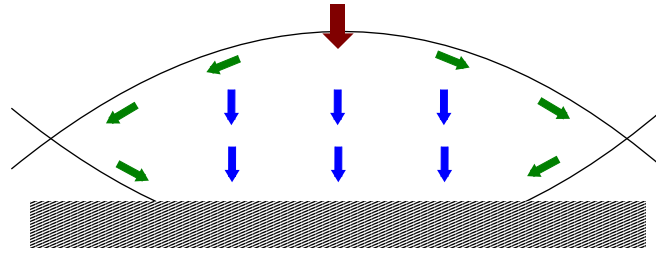


**Figure 12.** Sketch of the heat-flux in the SOL of W7-X. Depicted is the cross section of an island. The target is on the bottom. The heat-flux  $P_s$  is entering at the top (red arrow). The channel via parallel transport  $P_{\parallel}$  at the edge of the island is shown as green arrows, while the transport through the bulk of the island  $P_{\perp}$ , relying on diffusion, is shown as blue arrows.

### 5.1. Transport models

Besides scenario A: featuring constant diffusion, two different spatially varying diffusion coefficient distributions have been tested in EMC3-Eirene. The three scenarios have been used for a scan in both density as well as the magnitude of the diffusion coefficient, using the EMC3-Eirene code. A one-to-one comparison of the heat-flux from experiment and simulations were performed.

**5.1.1. Scenario B: experimentally motivated** Figure 12 sketches the simplified transport through the island in the island divertor on a single island. The heat from the confined region  $P_s$  enters the island through the separatrix, which separates the island from the confined region, depicted as a red arrow. This is not localised, but spread over the entire separatrix. From the region where the heat enters the island, there are, in a simple picture, two channels to the target: the parallel channel and the perpendicular channel. The parallel channel is depicted by green arrows in fig. 12. In tokamaks this is the main channel of transport in attached conditions and can be described by the two-point-model [27, 28, 29]. The heat-flux is described by the Spitzer conduction, scaling with temperature  $q \propto T^{5/2}$ , that is, a strong function of temperature. As  $T$  drops radially into the island the parallel transport becomes less efficient. Thus, only a width of the order of the temperature decay length  $\lambda_T$  contributes to the parallel channel. The width in turn is determined by the perpendicular heat transport  $\lambda_T \propto \chi_s$  at the island edge. Note, that in a more complete model,  $\chi_s$  needs to be replaced by a flux-tube averaged quantity. This gives a total power going through the parallel channel as  $P_{\parallel} \propto \chi_s \times T_s^{5/2}$ , with  $T_s$  the separatrix temperature. The transport through the bulk of the island, depicted in blue, in turn depends on the temperature at the separatrix. After the initial  $\lambda_T$ , a change in  $\chi$  does not directly affect the parallel heat-flux. Indirect effects do exist: For a given separatrix heat-flux  $P_s$ ,  $P_{\parallel}$  needs to decrease if  $P_{\perp}$  increases, resulting in a lower separatrix temperature  $T_s$ . These indirect can be significant. The heat-flux for a single perpendicular channel is proportional to the “integrated heat conductivity”:  $X = 1 / \int_{sep}^{tar} \frac{1}{\chi} dr$ . It is also proportional to the temperature difference between the temperature  $\lambda_q$  from the separatrix and the temperature at the PFC  $T \approx 0$ . Thus the temperature difference is  $T(R_{sep} + \lambda_T) - 0 = T_s/e \propto T$ . The total heat-flux through the bulk of the island  $P_{\perp}$  is given by the sum over all possible channels  $P_{\perp} \propto T_s \iint X dA$ . Thus increasing  $\chi$  in the bulk of the island, increases  $X$  and, thus,  $P_{\perp}$  without a direct effect on  $\lambda_T$ . This allows to retain the peak shape, but lower upstream temperature, as power is put into the far SOL. This is seen in the results for scenario B, where the enhanced transport towards the centre of the island retains a narrow SLW, but allows to decrease the separatrix temperature.

**5.1.2. Scenario C: turbulence scaling** Scenario C is based on the scaling of turbulent transport with bad curvature, which is in W7-X largest at the outer bean cross-section. Similar to scenario B, this scenario allows us to decrease the separatrix temperature, without a significant impact on the SLW. This is in contrast to scenario A, where the decoupling was not possible. The transport is enhanced at the edge of the separatrix, but not at, or below, the x-points, as shown in fig. 7. The main contribution to the parallel connection length is around the x-point. This could be an explanation why scenario C features a reduced upstream temperature and a narrow strike-line, increasing agreement with experimental measurements.

**5.1.3. Distinguishability of scenarios** The strike-line width from the experiments has been determined to be around 2 cm to 4 cm in the magnetic standard configuration. For all scenarios and densities, cases have been found that are consistent with the magnitude of the strike-line. The observed SLW of 2 cm to 4 cm is true for the low iota target, the high iota target as well as the vertical target, independent of the connection length. This observation is reproduced in the simulations, where for a given density and diffusion the strike-line width is roughly constant for all significantly loaded areas. As also the toroidal distribution features similar shape for all scenarios, it is not clear whether it is possible to distinguish the appropriate transport model based purely on the target profiles. The different scenarios show clearly different radial profiles at the line of sight of the MPM. For the density profiles, scenario B and scenario C show for large  $D$  values an increased density in the shadowed volume. Scenario B drops of sharply at the point where  $D$  is decreased again, while scenario C does not feature this drop, as the diffusion coefficient does not have a radial dependency. For the temperature profiles, more variation is observed. The temperature falloff length varies significantly between the different simulations. The shortest falloff length is observed for scenario A  $D = 0.1 \text{ m}^2/\text{s}$  while the largest falloff length is observed for scenario B  $D = 0.1 \dots 2.5 \text{ m}^2/\text{s}$ . None of the cases

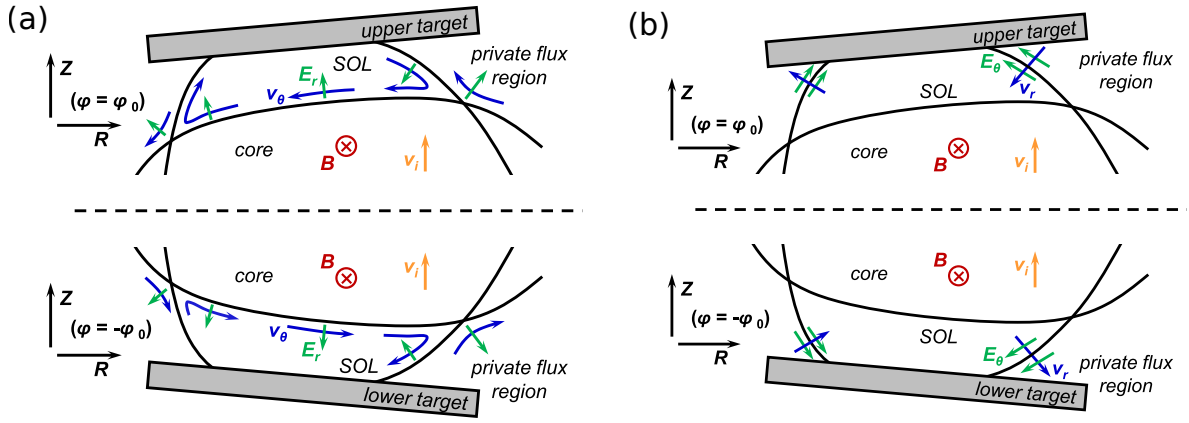


Figure 13. Sketch of the  $\vec{E} \times \vec{B}$  drifts in W7-X. Based on the work of Hammond et al. [9].

show good agreement with the measured profiles, as the experimental data shows vanishing gradients closest to the O-point, while the simulations all show a monotonic behaviour.

The inclusion of upstream measurements, like from the MPM, is crucial for accurately comparing transport models and experiments. This is due to the observed “insensitivity” of the target profiles to the different scenarios, where for all scenarios a good match with experiments has been found.

$D = 0.2 \text{ m}^2/\text{s}$  and  $n_{e,\text{sep}} = 1 \cdot 10^{19} \text{ m}^{-3}$  from scenario A matches the lower divertors. The upper divertor is better matched by an increased diffusion, case  $D = 0.5 \text{ m}^2/\text{s}$  and  $n_{e,\text{sep}} = 1 \cdot 10^{19} \text{ m}^{-3}$ , or increased density, case  $n_{e,\text{sep}} = 3 \cdot 10^{19} \text{ m}^{-3}$  and  $D = 0.2 \text{ m}^2/\text{s}$ . The up-down asymmetry reverses if the magnetic field is reversed [30], in line with the effects of drifts.

## 5.2. Drifts

Field errors could cause the variations between half modules, but the variation between upper versus lower half modules seems rather systematic, even after symmetrisation with error field correction [2]. Drifts are expected to cause up-down asymmetries as depicted in fig. 13 [9]. Experiments with reversed field can be used to test this hypothesis. Extending this analysis to low or high iota cases would also be interesting, as in those cases the impact of error fields is expected to reduce. However, due to the changed SOL geometry, the effect of drifts is also likely to change.

The location of the strike-line, shown in ref. [2], is in agreement with Hammond et al. [9] where, in the low iota forward configuration, the peak heat load on the low iota target was a few cm closer to the pumping gap compared to the magnetic strike line, which was attributed to drifts.

Experiments of field reversal in low iota configuration [9] and standard configuration [30] imply drifts are responsible for up-down asymmetries. The experiments include error field correction, i.e. the magnetic field has been optimised to minimise differences between the different target heat loads [24] and should thus be of reduced importance, leaving an exacerbated role for drifts. Besides drifts, a systematic misalignment of the divertors or vertical misplacement of the entire plasma could explain the up-down asymmetry.

**5.2.1. Impact of drifts on SLW** The strike-line width varied between upper and lower divertor [2]. If one assumes that this is based on drifts, one can make a rough estimate on the effective parallel drift velocity using a simple model: The parallel velocity is assumed to be the sound speed  $c_s$ , modified by the drift velocity, with the sign of the drift depending on upper or lower divertors. Rather than the actual drift velocity, the effective parallel drift velocity  $v_{D,\parallel}$ . The projection of  $v_{D,\parallel}$  on the perpendicular plane gives the drift velocity  $v_{D,\perp}$ . The estimated parallel transport time is then based on the parallel connection length  $L_{\parallel}$  and given by  $L_{\parallel}/(c_s \pm v_{D,\parallel})$ . This gives a strike-line width of around

$$\lambda_{\pm} \approx \sqrt{\frac{\chi L_{\parallel}}{c_s \pm v_{D,\parallel}}} \quad (1)$$

which in turn gives an effective drift speed of

$$v_{D,\parallel} \approx \frac{\chi L_{\parallel}}{2} \frac{\lambda_{-}^2 - \lambda_{+}^2}{\lambda_{+}^2 \lambda_{-}^2} \quad (2)$$

or an estimate of the heat diffusion  $\chi$

$$\chi \approx \frac{2c_s}{L} \frac{\lambda_{+}^2 \lambda_{-}^2}{\lambda_{+}^2 + \lambda_{-}^2} \quad (3)$$

Using  $\lambda_- = 3$  cm and  $\lambda_+ = 2$  cm, and assuming  $L_{\parallel} \approx 100$  m and  $\chi = 0.3$  m<sup>2</sup>/s this gives an effective parallel contribution of the drifts on the order of  $v_{D,\parallel} \approx 21$  km/s and, thus, in the range of the speed of sound, which is around 30 km/s. Using the velocity of 30 km/s gives  $\chi \approx 0.17$  m<sup>2</sup>/s and thus in the range that was used in the simulations.

As the field line pitch in W7-X is around 0.001, means that  $v_{D,\perp}$  is around 1000 times smaller than  $v_{D,\parallel}$ . Thus  $v_{D,\perp} \approx 21$  m/s and thus several orders of magnitude smaller than experimentally measured [31]. Thus it seems this simple SOL model for the impact of drifts on not valid. Reasons might be that the dwell time in the SOL is not set by the parallel dynamic, but rather by perpendicular process. This would be in contrast to tokamaks, where the field line pitch is much smaller.

**5.2.2. Toroidal distribution** While it is possible to match the strike-line width to the experimental ones, none of the simulations matched the toroidal distribution on the low iota target. The flattening with higher  $n$  and  $D$  is however observed in all cases. The toroidal distribution does not appear to be strongly influenced by the diffusion model chosen. There is a weak dependency on density and diffusion magnitude, which has already been discussed for scenario A [2].

Scenario B with  $n_{e,\text{sep}} = 3 \cdot 10^{19}$  m<sup>-3</sup> shows, compared to the other simulation, an increased heat-flux at  $\varphi \approx -17^\circ$ . However, a strong peaking, as in the experiments at  $\varphi \approx -17^\circ$  is not reproduced. As those field lines ending at  $\varphi \approx -17^\circ$  are in the private flux region (PFR), it requires additional perpendicular transport. That could be anomalous or drift driven. A toroidal redistribution of fluxes could be associated with  $E \times B$  drifts. That would require poloidal electric fields, that cause a radial drift into the PFR, as shown in fig. 13.

**5.2.3. Hollow island** The hollow temperature profile, as measured by the MPM in the island has not been reproduced by any of the simulations. In order to do so, a significant sink in the centre, e.g. due to radiation, or a significantly transport reduction into the centre is needed. The density profiles measured by the MPM agree better with the non-constant diffusion coefficients, selected from the simulation with a matching strike line width. The hollow temperature profile and the associated non-monotonic density profile in the island have been repeatedly experimentally observed in the past also by other diagnostics in different locations [22, 32, 33, 23, 11, 34, 31]. In EMC3-Eirene simulations, this has been reproduced by locally reducing the heat transport in the centre of the island. To reproduce a hollow temperature profile, the heat diffusion coefficient in the island needs to be reduced by an order of magnitude, and in order to get similar results to experiments by two orders of magnitude. It is not obvious why heat transport in the island centre should be that strongly suppressed. The lack of match in the here presented simulations shows that the current model are either missing a fast transport channel around the island centre, or a significant transport reduction into the island. The fast transport around the island would connect a region outside of the O-point to a point inside. This would allow to transport the heat around the island, without the heat going through the island centre.

To help elucidate how important drifts may be, we assume the hollow island is caused by fast convective transport around the island centre, and drifts are solely responsible for the convective transport. An estimate of the velocity can then be given. This assumes that the transport time is given by the square of the fall-off-length  $\lambda_T$  over the diffusion coefficient. For the poloidal convective transport to be sufficiently fast to compete with the diffusive inward transport, the poloidal transport needs to fulfil:

$$v_{pol} \gtrsim L_{pol} \chi \left( \frac{\nabla T}{T} \right)^2 \approx L_{pol} \chi \frac{1}{\lambda_T^2} \quad (4)$$

Using a falloff length of  $\lambda_T \approx 3$  cm, consistent with the data presented here, the poloidal island size  $L_{pol}$  on the order of one meter, and  $\chi \approx 0.3$  m<sup>2</sup>/s gives  $v_{pol} \gtrsim 300$  m/s. Parallel flow velocities observed by experiments and EMC3-Eirene are typically in the range of 30 km/s. The field line pitch is around 0.001, giving a perpendicular contribution of 300 m/s. This suggests that drifts could be comparable to parallel flows, which is in line with the above discussion. The estimate of  $\gtrsim 300$  m/s is however larger than the above estimated  $\approx 21$  m/s for the perpendicular velocity. The drift velocity measured by the MPM are consistent with this estimate [32]. This can also be incorporated into the two-channel model shown in fig. 12. Assuming a fast enough drift velocity within the island but outside of the power carrying layer,  $\chi$  can be increased ( $\rightarrow \infty$ ) by the part of the path that is governed by fast poloidal rotation and, thus, giving an effectively increased  $X$ . The motivation for such an assumption is, that if the drift is fast enough, this results in a constant temperature within the closed poloidal loop.

## 6. Conclusion and Summary

Please note that a short summary of the results is already given in sec. 4.6. As such only results are included, that are needed for the discussion.

The quantitative comparison performed here shows that, in order to reproduce the experimentally observed strike line width in the range of 2 to 4 cm, diffusion coefficients of 0.2 m<sup>2</sup>/s around the separatrix are needed in the magnetic standard configuration for low to medium density cases. In addition to constant diffusion coefficients, spatially varying diffusion coefficients can be used to reproduce the experimentally observed strike-line width. The main features at the target, namely SLW and toroidal distribution, were not strongly sensitive to the chosen transport model at moderate values of  $D$ . This allows to tune the magnitude of the spatially varying diffusion coefficients to match other quantities, in this case to reduce the separatrix temperature.

There are significant differences between simulations and experiments, that could not be reproduced by the simulations, even using strongly spatially varying diffusion coefficients. Some differences are expected to be due to, or seem to be consistent with, a lack of drifts in EMC3-Eirene: e.g. the up-down asymmetry on the divertor target plates, the hollow island or the too high upstream temperature. Other discrepancies remain which are not expected, such as the difference in the toroidal distribution of the heat-flux which peaks at  $\varphi \approx -17^\circ$  on the low iota target. Additionally, hollow temperature profiles in the islands are measured by probes and other diagnostics, which has not been reproduced by the simulations. Non-isotropic transport in the perpendicular plane could help to reproduce this, but convective perpendicular transport due to drifts would also be in agreement with the experimental measurements.

Altogether, these observations show that spatially varying diffusion coefficients can improve agreement to experimental measurements, but so far the applied variations have not been able to match experimental measurements consistently up and downstream. The observed discrepancies and experimental measurements further indicate that drifts could contribute substantially to the transport in W7-X, which cannot be captured with the present version of EMC3-Eirene. Thus, implementation of the drifts are a priority for future work in order to fully capture the physics seen in experiments and determine if they are sufficient to explain the discussed discrepancies.

## 7. Acknowledgement

This work has been carried out using the xarray framework [35, 36]. Some tasks have been parallelised using GNU parallel [37].

The simulation presented here are available at: DOI: 10.5281/zenodo.5762079

This work has been carried out within the framework of the EUROfusion Consortium, funded by the European Union via the Euratom Research and Training Programme (Grant Agreement No 101052200–EUROfusion). Views and opinions expressed are however those of the author(s) only and do not necessarily reflect those of the European Union or the European Commission. Neither the European Union nor the European Commission can be held responsible for them.

- [1] PEDERSEN, T. S. et al., Nuclear Fusion **62** (2022) 042022.
- [2] BOLD, D. et al., Nuclear Fusion **62** (2022) 106011.
- [3] KLINGER, T. et al., Plasma Physics and Controlled Fusion **59** (2017) 014018.
- [4] WOLF, R. et al., Nuclear Fusion **57** (2017) 102020.
- [5] SUNN PEDERSEN, T. et al., Physics of Plasmas **24** (2017) 055503.
- [6] BEIDLER, C. D. et al., Nature (2021).
- [7] PEDERSEN, T. S. et al., **61** (2018) 014035.
- [8] PEDERSEN, T. S. et al., **59** (2019) 096014.
- [9] HAMMOND, K. C. et al., **61** (2019) 125001.
- [10] KILLER, C. et al., **62** (2020) 085003.
- [11] KILLER, C. et al., **61** (2021) 096038.
- [12] ZOLETNIK, S. et al., Plasma Physics and Controlled Fusion **62** (2019) 014017.
- [13] LIU, S. et al., Nuclear Fusion **59** (2019) 066001.
- [14] WINTERS, V. R. et al., Plasma Physics and Controlled Fusion **63** (2021) 045016.
- [15] LUNT, T. et al., **62** (2020) 105016.
- [16] ZHANG, W. et al., Nuclear Fusion **56** (2016) 036007.
- [17] CARLI, S. et al., Contributions to Plasma Physics **60** (2020) e201900155.
- [18] FENG, Y. et al., Contributions to Plasma Physics **54** (2014) 426.
- [19] FENG, Y. et al., Nuclear Fusion **61** (2021) 086012.
- [20] JAKUBOWSKI, M. et al., Review of Scientific Instruments **89** (2018) 10E116.
- [21] SIEGLIN, B. et al., Review of Scientific Instruments **86** (2015) 113502.
- [22] KILLER, C. et al., **59** (2019) 086013.
- [23] KILLER, C. et al., Journal of Instrumentation **17** (2022) P03018.
- [24] LAZERSON, S. A. et al., **60** (2018) 124002.
- [25] FENG, Y. et al., Nuclear Fusion **61** (2021) 106018.
- [26] SCHWÖRER, D. et al., Plasma Physics and Controlled Fusion **61** (2018) 025008.
- [27] BORRASS, K., Nuclear Fusion **31** (1991) 1035.
- [28] PITCHER, C. S. et al., Plasma Physics and Controlled Fusion **39** (1997) 779.
- [29] SCHWÖRER, D., *On the influence of background including neutrals on the dynamics of 3D scrape-off layer filaments in fusion devices*, PhD thesis, Dublin City University, Ireland, 2020.
- [30] ZHANG, D. et al., Nuclear Fusion **61** (2021) 116043.
- [31] FLOM, E. et al., Observation of a drift-driven local transport regime in the island divertor of wendelstein 7-x, 2023.
- [32] KILLER, C. et al., **61** (2019) 125014.
- [33] DREWS, P. et al., Nuclear Materials and Energy **19** (2019) 179.
- [34] BARBUI, T. et al., (2019).
- [35] HOYER, S. et al., Journal of Open Research Software **5** (2017).
- [36] HOYER, S. et al., <https://doi.org/10.5281/zenodo.4563695>, pydata/xarray: v0.17.0, 2021.
- [37] TANGE, O., *GNU Parallel 2018*, Ole Tange, 2018.